

Bianca Omede'1 & Antonio Mattia Grande1

<sup>1</sup> Department of Aerospace Science and Technology, Politecnico di Milano, Via La Masa 34, 20156 Milan, Italy

## **Abstract**

The present study aims to design an efficient elytra-inspired honeycomb cell structure for enhanced energy absorption. Various regression models are evaluated and then integrated into a metamodel for multiobjective optimisation. Multivariate Polynomial Regression (MPR), Linear Ridge Regression (LRR), Kernel Ridge Regression (KRR) and Deep Neural Network (DNN) regression models were evaluated. The LRR and DNN models were selected to be coupled with a genetic algorithm (NSGA-II) for multi-objective optimisation aimed at minimising peak crushing force and maximising Specific Energy Absorption (SEA), while also considering Crushing Force Efficiency (CFE). The DNN-derived configuration showed the highest SEA (+106.2%) and CFE (+37.3%). While the LRR model proved to be faster (5.3 s vs. 868 s), the DNN model provided higher accuracy with significantly lower mean relative errors between the values determined by the FEA and the metamodel (18.54% and 6.83% vs. 1.39% and 2.0% for peak force and SEA, respectively). The combined DNN/NSGA-II metamodel was  $10^4$  times faster than the conventional finite element analysis. It proved to be effective for initial structural optimisation and provides a cost-effective approach for advanced structural engineering solutions.

**Keywords:** Deep Neural Networks (DNN), Finite Element Analysis (FEA), Bio-inspired structure, Multi-Objective optimization, Crashworthiness

## 1. Introduction

The demand for lightweight structures with high energy absorption capacity has increased significantly in areas such as aerospace, transport, nuclear reactors and construction [1]. To meet this demand, various energy absorbers with different structures have been tested to reduce weight while improving safety and functional properties in the event of a direct axial impact [2].

Nature-inspired and biomimetic geometries exhibit remarkable efficiency and versatility, optimally utilising materials and structures to perform in demanding environments. These geometries, which incorporate design concepts such as structural hierarchies, density gradients and thin-walled tubular/cellular structures, combine lightweight properties with impact resistance [3]. In aerospace, lightweight, low-density structures, such as sandwich structures, play an important role in ensuring compressive strength in impact scenarios. These structures, which often contain foam, lattice or truss cores, offer a low weight-to-area ratio while ensuring stiffness, strength and absorption of impact energy [4]. Additive Manufacturing (AM) contributes to passive safety in aviation by reducing production costs and enabling higher design complexity [5]. Various bio-inspired structures have already been pro-

Additive Manufacturing (AM) contributes to passive safety in aviation by reducing production costs and enabling higher design complexity [5]. Various bio-inspired structures have already been produced using 3D printing technologies and show excellent energy absorption properties, especially those inspired by insect wing covers [1, 6]. The geometries and structures described in this article appear to be particularly well suited to this particular manufacturing process.

Optimising the impact behaviour and energy absorption of structures is an important research focus that benefits public safety and the economy as a whole [7]. Engineers use Computer-Aided Engineering (CAE) design software and simulation tools, such as Finite Element Analysis (FEA) packages, to predict the performance of lightweight structures before production [8]. However, direct non-linear FEA can be resource intensive. As an alternative, surrogate models or metamodels that express

design criteria in the form of an explicit function of the design variables prior to optimisation are often used [7]. This approach has proven successful for applications in the field of structure and crash behaviour [9, 10, 11].

Artificial Intelligence (AI), particularly Machine Learning (ML) and Deep Learning (DL), has become a powerful tool for predicting non-linear properties and optimising structures. ML uses algorithms and analytics to create predictive models by analysing large datasets and identifying patterns and rules using various techniques, and serves as a cost-effective replacement for FEA. A widely accepted approach involves a two-step process: model approximation using an Artificial Neural Network (ANN) and variable optimisation using a Multi-Objective Optimization (MOO) algorithm [12]. This combination has proven to be efficient in predicting optimal structures, especially when combined with genetic algorithms [14, 15].

The integration of DL into structural optimisation leads to new perspectives and refinements in data regression approaches. In contrast to traditional models, DL can handle complex, non-linear relationships more accurately and dynamically adapts to changes in structural parameters, leading to improved prediction accuracy. This research presents an alternative to standard surrogate structural optimisation that builds on the results of a previous study [16] and compares traditional methods with DL-based approaches.

The paper is organised as follows: Section 2 presents the optimisation methods used. Section 3 presents and discusses the results, focusing on the comparison between the results obtained with classical polynomial regression and those obtained with DL algorithms. Finally, the conclusions are presented in Section 4.

## 2. Materials and methods

## 2.1 Structural crashworthiness indices

The criteria for quantitatively evaluating the crashworthiness of different structures are determined using the force-displacement profile of an energy absorber subjected to either crushing force or controlled displacement, as defined in the literature [1]. Key parameters include the axial crushing force F(x) as a function of the displacement x, the effective deformation distance  $d_{max}$ , the maximum crushing force  $(F_{max})$  and energy absorption (EA). Four indicators are used to define crashworthiness performance [17]:

Energy absorption (EA):  $EA(d) = \int_0^{d_{max}} F(x) dx$ . This evaluates an energy absorber's ability to dissipate crushing energy through plastic deformation, represented by the area under the force-displacement curve.

Specific Energy Absorption (SEA): SEA(d) = EA(d)/M. This is the ratio of the EA of a structure to its mass (M), allowing comparison of energy absorption performance across different materials and structures.

*Mean crushing force*  $(P_m)$ :  $P_m = EA(d)/d_{max}$ . This is the average compressive force exerted by the energy absorber over the entire effective deformation distance.

Crush Force Efficiency (CFE):  $CFE = P_m/F_{max}$ . This indicator measures the uniformity of the load during energy absorption. A higher CFE value indicates minimal changes in the energy absorption mechanism during deceleration, which is beneficial for reducing potential damage to passengers or other payloads.

# 2.2 Feed-Forward Neural Networks (FFNN)

Feed-Forward Neural Networks (FFNNs) are a type of DL artificial nerual network commonly used for creating input-output relationships and they are inspired by the structure of the human brain [18]. Each input parameter  $x_i$  is multiplied by a corresponding weight  $w_i$ , adjusted with a bias b and then summed to a unit known as a neuron. Fig. 1 shows a diagram of a neuron with multiple weighted inputs. Each neuron consists of a basic processing operation with the inherent ability to store information about the weights [18]. The output of the neuron, y, is determined by an activation function  $\mathscr{F}$  such that  $y = \mathscr{F}(w_i x_i + b)$ .

A typical neural network can receive multiple input signals from different channels, process these inputs using the weights and biases of the network, and incorporate nonlinear factors via the activation

function. By adding nonlinearity, the neural network can approximate any nonlinear function and improve the overall robustness of the network. In a FFNN, a different number of neurons are connected to the same set of input parameters via corresponding weights and bias values. The output of these neurons is passed to another layer of neurons via an activation function, forming a multi-layer neural network. Common activation functions include the Rectified Linear Unit (ReLU), the sigmoid function, Softmax and the hyperbolic tangent function (Tanh). This structure creates a multilayer FFNN in which each input is passed through the neurons to the corresponding hidden layers without feedback. Fig. 2 shows a schematic representation of such a network. As shown, each hidden layer contains neurons that are connected to the next hidden layer via unique weights and bias matrices. These weights and biases are adjusted to minimise a loss function that measures the difference between the predicted output and the actual output of the network. The learning algorithm calculates the gradient of the loss function with respect to the weights and biases of each hidden layer through backpropagation and then uses optimisers to minimise this loss. Common loss functions include Mean Squared Error (MSE), Mean Absolute Error (MAE) and Cross Entropy Loss. Commonly used optimisation algorithms are Stochastic Gradient Descent (SGD), Levenberg–Marquardt, RMSprop and Adam [8].

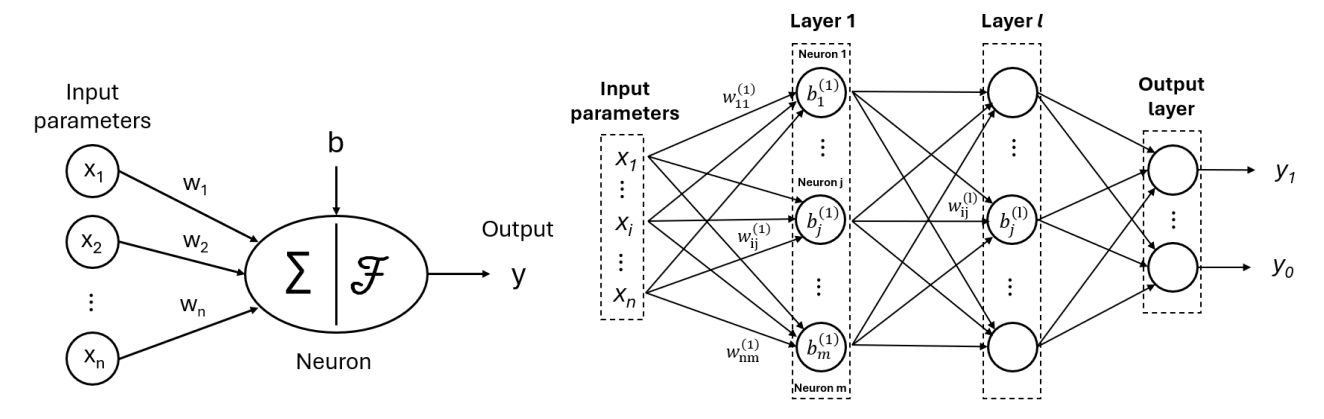


Figure 1 – Scheme of a single neuron with multiple weighted input.

Figure 2 – Scheme of a feed-forward multi-layered neural network.

## 2.3 Crashworthiness optimization framework methodology

The objective of this work is to identify the structure that demonstrates the best crashworthiness performance when subjected to an axial impact load. The optimisation flow followed in this work is shown in Fig. 3. The comparison of different geometries inspired by elytra was performed using the COPRAS methodology, leading to the selection of the best candidate structure for subsequent optimisation. Then, multi-criteria optimisation approach for the selected structure is performed, which integrates NSGA-II, the response surface method and FE modelling under dynamic impact loading conditions. This follows a Design Of Experiment (DOE) approach. Section 3 discusses the results of the optimisation.

## 2.4 Selected geometries and COPRAS results

Previous work [16] drew inspiration from insect wings, specifically elytra, to develop geometries with high energy absorption capacity. Two preliminary geometries were analyzed: one with a circular main structure and reinforcing cylinders, and one with linear walls (polygonal shape) and reinforcing cylinders positioned at the polygon edges. The

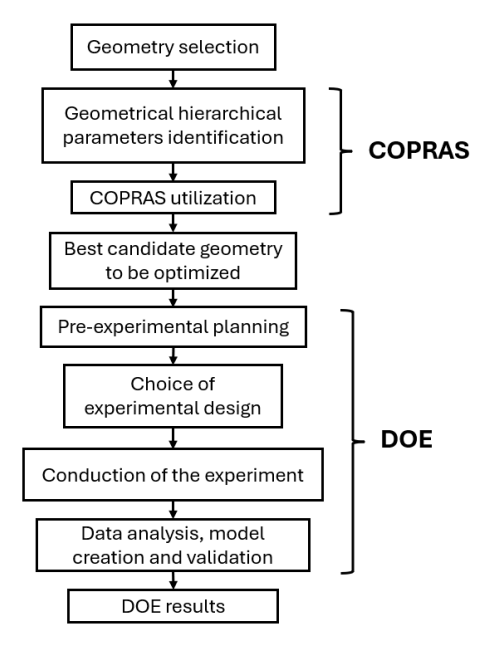


Figure 3 – Crashworthiness optimization framework flowchart.

analysis considered geometries with a maximum circumference and height of 50 mm, calculating energy absorption up to a 20 mm compression.

To compare the structures, the COmplex PRoportional ASsessment (COPRAS) method was used [19, 9]. COPRAS is a Multi-Criteria Decision Making (MCDM) methodology that evaluates and selects the best option based on conflicting criteria. In this case, energy absorption (EA) and crushing force efficiency (CFE) were maximized, while peak compression force ( $F_{max}$ ) was minimized. The COPRAS method identified the circular configuration with 4 reinforcing cylinders (C4) as the best. This configuration demonstrated a 68.4% higher specific energy absorption (SEA) than a simple hollow metal cylinder with same dimensions and mass (refer to Fig. 5 and Tab. 1) and demonstrated a progressive deformation mode, which reduces fluctuations in the crushing force (Fig. 4). The C4 geometry was therefore selected for multi-objective optimization to be performed in the current work.

| Geometry           | SEA [J/g] | $F_{max}$ [kN] | EA [kJ] | CFE [-] |
|--------------------|-----------|----------------|---------|---------|
| Reference cylinder | 19.38     | 215.53         | 3.04    | 0.6701  |
| C4                 | 32.65     | 285.22         | 5.14    | 0.8671  |
| % variation        | +68.47%   | +32.33%        | +69.08% | +29.40% |

Table 1 – Design variables comparison for C4 COPRAS results.

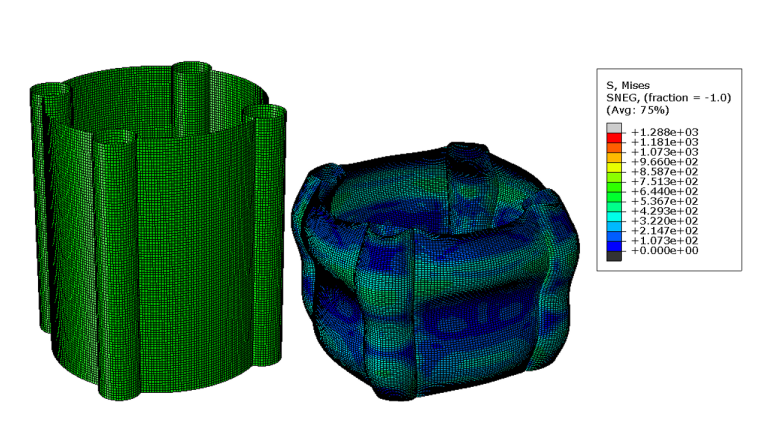


Figure 4 – Undeformed and deformed shapes of C4 investigated with the COPRAS methodology.

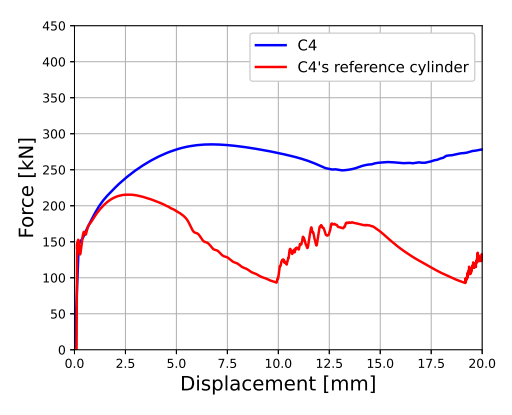


Figure 5 – C4's force-displacement graph comparison with reference cylinder.

## 2.5 Design of Experiments (DOE) approach

According to the comparative analyses mentioned above, structure C4 performs best from a multi-criteria point of view and under axial impact loading. Therefore, a multi-criteria optimisation was performed to find the best possible design. Numerous non-linear FE simulations are normally carried out to optimise crashworthiness. Surrogate modelling has established itself as an efficient method for solving this problem. A Design of Experiment (DOE) is a widely used technique for structural optimisation in an initial design phase, as design of experiment plays a crucial role in optimising production processes in science and engineering. It can lead to reduced variability, better compliance with target requirements, shorter development times and lower overall costs when performed in the early stages of process development [21]. The DOE approach consists of the following four steps: 1) Pre-experimental planning, 2) Choice of experimental design, 3) Conduction of the experiment, 4) Data analysis, modelling and validation. The individual phases are explained in more detail in the following sections.

## 2.5.1 Pre-experimental planning

The first step in multi-criteria optimisation was to identify the response variables and the geometric factors with their ranges. The geometric design factors are the variables that were varied during

the experiment and were thus considered as input factors that influence the performance of the system. In this case, the response variables of interest were the maximum crushing force  $(F_{max})$ , which should be minimised as excessive impact force can lead to significant deceleration that could result in serious injury or even death to the occupants, and the specific energy absorption (SEA), which should instead be maximised as the primary goal for an energy absorber is to maximise its energy absorption capacity [22].

The selected design variables, which instead represent geometric parameters that are varied to create different geometries, include the wall thickness ( $t_w$ ) in the range of 1 to 2.5 mm, the thickness of the reinforcing cylinders ( $t_c$ ) in the range of 1 to 2.5 mm, the radius of the reinforcing cylinders (r) within 2.5 to 6 mm (where the maximum outer diameter is fixed, which affects the variation of the diameter of the main feature) and a parameter of the leading line of the deformations. Regarding this last variable, according to some studies [23], the mechanical properties of a crash box can be adapted to different technical requirements by varying the amplitude of the deformation lines. These results inspire the application of bionic structures based on beetle elytra and the use of new buffer structures to mitigate the damaging effects of collision events and improve crashworthiness safety. A sinusoidal deformation line of the form  $Z = A \sin(0.3 \times X)$  was implemented along the height of the structure to investigate these effects. Here, A is a parameter that controls the amplitude (in the range from 0 to 1.5) of the sinusoidal function, while the periodicity is kept constant with a parameter equal to 0.3.

To summarise, this study dealt with 2 response variables and 4 design variables whose ranges were selected according to possible manufacturing (e.g. the lower limits for the thicknesses), geometric (e.g. for *A*) and common-sense limits. The mathematical formulation of the optimisation problem can be given as Eq. 1:

$$\begin{cases} \text{Min} & F_{max}(t_w, t_c, r, A) \\ \text{Max} & SEA(t_w, t_c, r, A) \\ \text{s.t.} & 1.0 \le t_w, t_c \le 2.5 \\ & 2.5 \le r \le 6.0 \\ & 0.0 \le A \le 1.5 \end{cases}$$
 (1)

## 2.5.2 Choice of experimental design

Optimal Latin Hypercube Sampling (OLHS) [9] is an advanced sampling technique used to select an optimised set of points within a Latin hypercube. It is a variant of Latin Hypercube Sampling (LHD), but it aims to further improve the coverage and efficiency of parameter space exploration. OLHS was used to generate 150 training points that were tested in the next phase of the DOE.

## 2.5.3 Conduction of the experiment

Once the DOE test points were selected, the configurations corresponding to the selected design variables were simulated by computational experiments using Abaqus/CAE Explicit Solver. The simulations were carried out according to the same procedure described in Ref. [16] to obtain the COPRAS-optimal geometry. The force-displacement diagrams and mass properties were saved for each simulation performed so that the desired values for SEA and  $F_{max}$  could be calculated.

## 2.5.4 Data analysis, modelling and validation

Once the simulation data had been collected, the next step was to create a regression model to analyse the sample data. This model should fit the data to reveal the relationship between a response variable and the independent geometric factors. To achieve this, four different supervised ML algorithms are used for training, fine-tuning and testing. These algorithms are Multivariate Polynomial Regression (MPR), Linear Ridge Regression (LRR), Kernel Ridge Regression (KRR) and a Deep Neural Network (DNN). The numerical dataset used to tune the ML algorithms is divided into three segments: the training set (104 data points, i.e. 70% of the entire dataset), the validation set (23 data points, i.e. 15% of the entire dataset). The training set is used to help the ML algorithms learn the parameters that define the

regression models, in particular to establish the relationship between the input design variables  $(x_i)$  and the output crashworthiness indicators  $(y_i)$ . The validation and test sets serve different purposes: the former is used to fine-tune the hyperparameters of the algorithms, while the latter is used to evaluate the quality of the approximation, as it has never entered in the model fitting cycle. Following this process, the optimal metamodel is determined and then used in the genetic algorithm to calculate the mechanical properties of non-FE simulated geometric models. Fig. 6 illustrates the workflow used in this process.

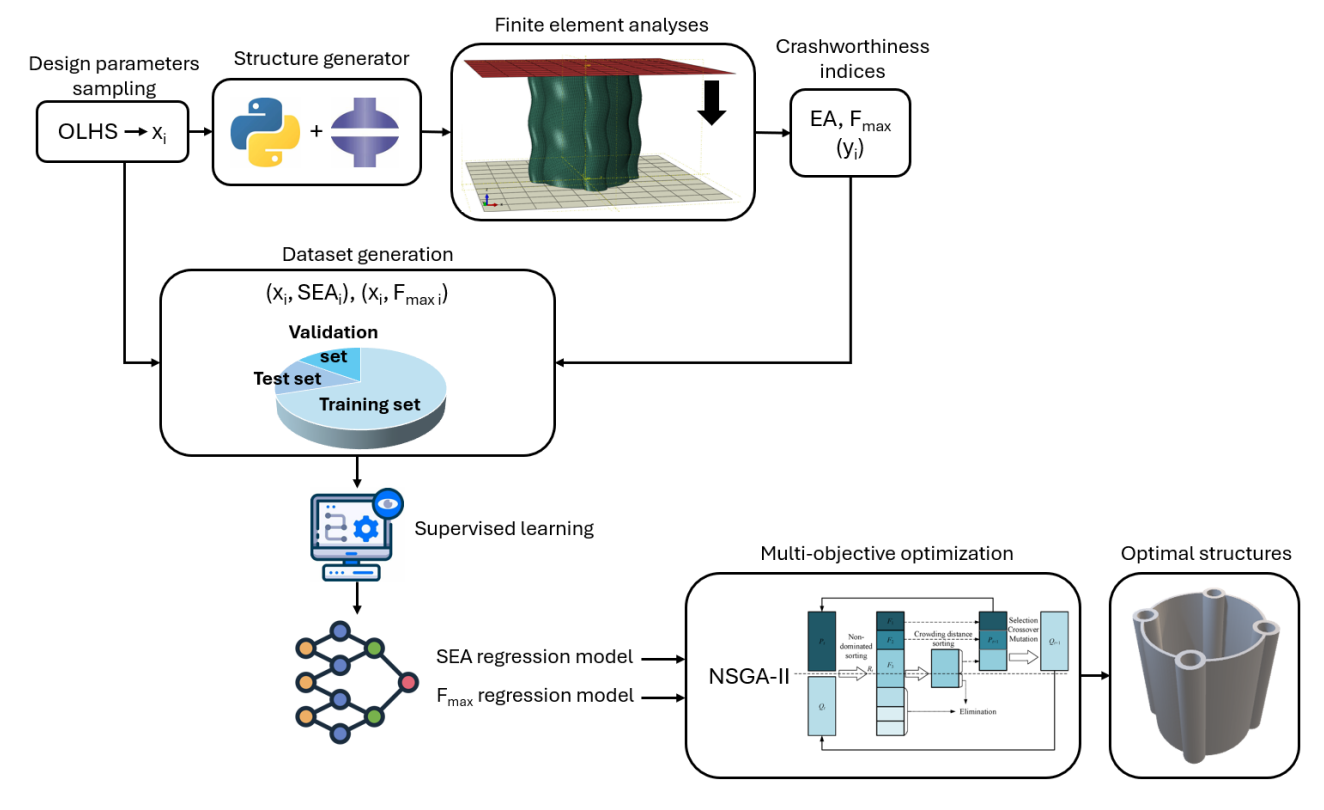


Figure 6 – The workflow diagram illustrates the process used in the DOE to create the numerical dataset, train the DL algorithms, predict the crashworthiness indices of the structures and perform a multi-objective optimisation through a genetic algorithm to obtain optimal geometries.

Two regression models were required: one for the maximum crushing force and one for the specific energy absorption. All input and output parameters are normalised between 0 and 1 to avoid any bias due to the different scales of the parameters and thus improve the performance of the ML algorithms. The data normalisation processing method is illustrated by the following equations:

$$\bar{x}_{i}^{(d)} = \frac{x_{i}^{(d)} - \min(x_{i})}{\max(x_{i}) - \min(x_{i})} \quad , \quad \bar{y}_{SEA}^{(d)} = \frac{y_{SEA}^{(d)} - \min(y_{SEA})}{\max(y_{SEA}) - \min(y_{SEA})} \quad , \quad \bar{y}_{F}^{(d)} = \frac{y_{F}^{(d)} - \min(y_{F})}{\max(y_{F}) - \min(y_{F})}$$
(2)

where i represents the i-th input parameter (i=1,...,4), d denotes the d-th design sample (d=1,...,150),  $\bar{x}_i^{(d)}$  represents the normalised value of the i-th input feature of the d-th input sample;  $x_i^{(d)}$  is the value of the i-th input feature of the d-th input sample;  $\bar{y}_{SEA}^{(d)}$  and  $\bar{y}_F^{(d)}$  denote the normalised value of the output parameters SEA and  $F_{max}$  of the d-th output samples, respectively;  $y_{SEA}^{(d)}$  and  $y_F^{(d)}$  denote the value of the output SEA and  $F_{max}$  output parameters of the d-th output samples, respectively;  $\min(x_i)$ ,  $\min(y_{SEA})$ ,  $\min(y_F)$ ,  $\max(x_i)$ ,  $\max(y_{SEA})$  and  $\max(y_F)$  denote the minimum and maximum values of all input features, SEA and  $F_{max}$  output values, respectively.

Four different supervised learning approaches are used and compared [24]:

• Multivariate Polynomial Regression (MPR): MPR is an extension of linear regression that allows for multiple input variables and non-linear (polynomial) relationships between the input variables and

the target variable. A degree of 3 was used for the polynomial equation for both the SEA and the  $F_{max}$  models.

- Linear Ridge Regression (LRR): LRR is chosen due to its simplicity and computational efficiency. Linear regression with L2 regularisation is used as an approximation tool. The implementation uses the corresponding Python package Scikit-learn, whereby a regularisation parameter  $\alpha=0.1$  was chosen to prevent underfitting.
- Kernel Ridge Regression (KRR): KRR is used to capture complex input-output relationships using nonlinear kernel algorithms while maintaining high computational efficiency. In this approach, we define a kernel regression model based on Radial Basis Functions (RBF) by utilising the capabilities of Scikit-learn. The regularisation strength  $\alpha$  and the hyperparameter  $\gamma$  associated with RBF were set to 0.1.
- Deep Neural Network (DNN): DNNs are chosen for their ability to approximate functions without limits[18]. However, compared to previous approaches, they require a significantly higher computational effort for training and hyperparameter selection due to the large number of parameters and hyperparameters that need to be tuned. In this project, we develop our own DNN with Keras, a user-friendly front-end API for TensorFlow. The two chosen DNN architectures include an input layer with 4 neurons (one for each design variable), an output layer with one neuron (SEA and  $F_{max}$ are predicted by different models), and 3 and 2 fully connected hidden layers with 256 neurons each for the models of SEA and  $F_{max}$ , respectively. A uniform variance scaling of He was used to initialise the weights of the hidden layers, while a uniform initialiser of Glorot was used to initialise the output layer. L2 regularisation was also used to regularise the kernel weight matrix of the hidden layer. The Exponential Linear Unit (ELU) activation function is applied to all layers except the output layer, where a "linear" activation function is used, which is commonly used for regression tasks in the last layer. ELU was chosen instead of the classical ReLU to avoid the vanishing gradient problem and to speed up the learning process as it brings the mean activation closer to zero [25]. Finally, the Adam optimisation algorithm is used to minimise the Mean Absolute Error (MAE) loss function. The training of the DNNs and their parameters comprises a total of 2000 epochs with a batch size of 16, taking into account early stopping and a reduction of the learning rate in case of plateau callbacks.

In order to verify the robustness and goodness of fit of the models and to ensure a robust agreement between the data obtained from the experiments and the data derived from the regression, two parameters had to be calculated and checked: the relative error and the value assumed by the coefficient of determination [26], which are respectively defined as follows:

$$R_e = \left| \frac{f_{fem}(\mathbf{x}) - f_{fit}(\mathbf{x})}{f_{fem}(\mathbf{x})} \right| \tag{3}$$

$$R^{2} = 1 - \frac{\sum_{i=1}^{N} (z_{i} - \hat{y}_{i})^{2}}{\sum_{i=1}^{N} (\hat{y}_{i} - \bar{z})^{2}}$$

$$\tag{4}$$

 $R^2$  normally ranges from 0 to 1 and it serves as an indicator of how effectively a statistical model can predict an outcome. On this scale, a value of 1 means a perfect match with the available data. In Eq. 4,  $\bar{z}$  is defined as the mean value of the simulated response z, while  $\hat{y_i}$  is the predicted value. Subsequently, the Non-dominated Sorting Genetic Algorithm (NSGA-II) [27] was used in multi-objective optimisation to identify a Pareto-Optimal (PO) front that represents the best and optimal solutions. It was chosen because it has the lowest possible computational complexity that can be achieved with any non-dominated sorting approach, namely  $O(MN^2)$ , where M is the number of objectives and N is the population size, and because it has been shown to be effective in solving problems of optimising the crashworthiness of energy-absorbing structures [22, 28]. Two performance metrics were used to evaluate the performance and correct functioning of the algorithm: the hypervolume and the running performance metric [29]. The hypervolume metric quantifies the area dominated by the given set of solutions relative to a reference point. Maximising this performance metric is desirable and it is usually between 0 and 1 when the response variables are normalised. In contrast, the running

metric evaluates the improvement of the PO front from one generation to the next. It compares the non-dominated points of one generation with those of the following generation, providing insight into the progress of the algorithm without requiring knowledge of the true PO front. This metric is used to determine whether and at which iteration the algorithm converges. The population size is set to 150 individuals, with 40 offspring generated per iteration. New individuals are generated by a random selection of floating point numbers. To combine individual traits, the algorithm uses simulated binary crossover and polynomial mutation to change individual characteristics. To ensure diversity within the population, duplicate individuals are removed.

## 3. Results and discussion

## 3.1 Regression models evaluation

Firstly, a sensitivity analysis was conducted on the size of the dataset and the corresponding performance of the model to determine the appropriateness of the DOE dataset size. Starting with a complete dataset of 25 simulations, the dataset size was gradually increased in increments of 25 up to 150, maintaining the division into training, test and validation sets as specified in Section 2.5.4 . The coefficient of determination calculated when fitting the test dataset, which is considered the most meaningful value, was chosen as the reference measure of performance. Tab. 2 shows the  $R^2$ values for different models and dataset sizes. It is noticeable that a dataset of 25 samples is clearly insufficient, as the coefficient of determination  $R^2$  is even negative, indicating that the predictions of the MPL and LRR SEA models are worse than a constant function that always predicts the mean of the data. Furthermore, it is evident that especially for the neural network regression model, an increase in the size of the dataset leads to an increase in  $R^2$  for both the SEA regression model and the  $F_{max}$  regression model. This trend is also recognisable for the LRR model of SEA and the MPR model of  $F_{max}$ . However, for the other models, with the exception of the 25-sample dataset, this behaviour does not appear to be as pronounced, but  $R^2$  immediately stabilises around a constant value. Fig. 7 shows, among other things, the trend of the training time for the DNN model of SEA and  $F_{max}$ : The former exhibits an increasing trend with the number of data points in the entire dataset, while the training time of the latter remains approximately constant. The training times of the MPL, LRR and KRR models were not reported in the figure because, as shown in Tab. 3, where the training times with 150 DOE samples are given, they are negligible compared to those of the DNN. Considering the highlighted coefficients of determination and training times, it was determined that 150 samples are appropriate for the DOE to be developed. Additional simulations would lead to an unwarranted increase in the training times of the DNN regression models without a corresponding increase in  $\mathbb{R}^2$ , which appears to stabilise around a constant value.

Table 2 – Table of  $R^2$  values for different models and dataset sizes.

| Dataset size | $R^2$ of S | EA regre | ssion mo | del [-] | $R^2$ of | $R^2$ of $F_{max}$ regression model [ |        |        |
|--------------|------------|----------|----------|---------|----------|---------------------------------------|--------|--------|
|              | MPL        | LRR      | KRR      | DNN     | MPL      | LRR                                   | KRR    | DNN    |
| 25           | -1.0952    | -0.2171  | 0.9262   | 0.5097  | 0.9903   | 0.9879                                | 0.7851 | 0.4611 |
| 50           | 0.9795     | 0.9343   | 0.9712   | 0.8995  | 0.7934   | 0.9981                                | 0.9787 | 0.9692 |
| 75           | 0.9726     | 0.9862   | 0.9195   | 0.9538  | 0.9881   | 0.9948                                | 0.9078 | 0.9788 |
| 100          | 0.8825     | 0.9670   | 0.8981   | 0.9656  | 0.9927   | 0.9967                                | 0.9593 | 0.9831 |
| 125          | 0.9913     | 0.9973   | 0.9794   | 0.9866  | 0.9957   | 0.9981                                | 0.9628 | 0.9770 |
| 150          | 0.9797     | 0.9835   | 0.9646   | 0.9941  | 0.9891   | 0.9880                                | 0.9708 | 0.9894 |

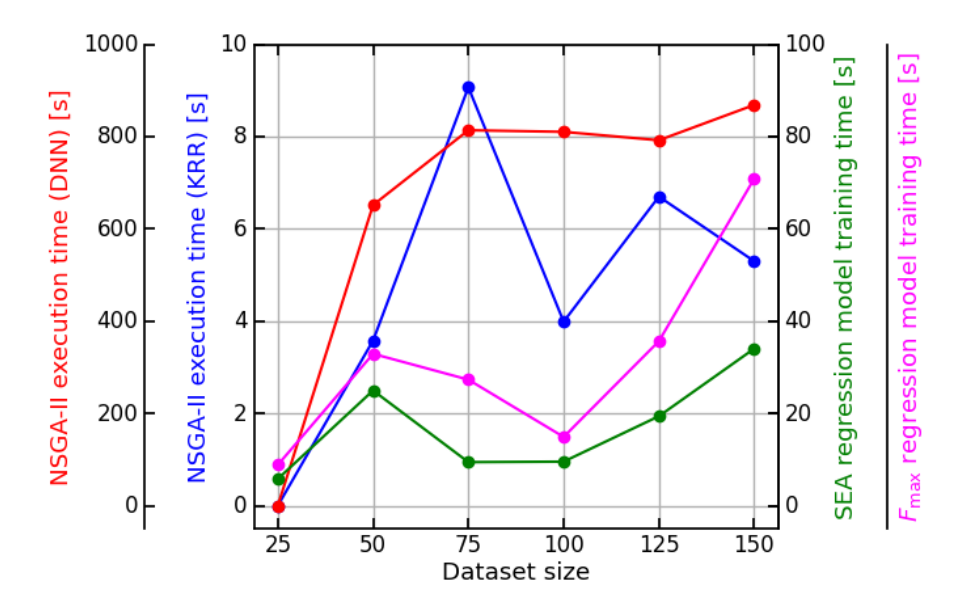


Figure 7 – Training times of the DNN models of SEA and  $F_{max}$ , and execution times of the NSGA-II metamodels coupled with DNN and KRR as a function of the number of samples in the entire dataset.

Table 3 – Coefficient of determination  $R^2$ , maximum relative error  $R_e$ , and training time of the MPL, LRR, KRR, and DNN models of SEA and  $F_{max}$ .

|       |                | SEAı      | regression     | model    | $F_{max}$ r | $F_{max}$ regression model |          |  |  |
|-------|----------------|-----------|----------------|----------|-------------|----------------------------|----------|--|--|
|       |                | $R^2$ [-] | $R_{emax}$ [%] | Time [s] | $R^2$ [-]   | $R_{emax}$ [%]             | Time [s] |  |  |
| MPL   | Training set   | 0.9939    | 11.18          | <0.001   | 0.9992      | 7.50                       | 0.003    |  |  |
| model | Test set       | 0.9797    | 8.98           | -        | 0.9891      | 14.19                      | -        |  |  |
|       | Validation set | 0.9801    | 9.38           | -        | 0.9976      | 4.26                       | -        |  |  |
|       | Complete set   | 0.9904    | 11.18          | -        | 0.9980      | 14.19                      | -        |  |  |
| LRR   | Training set   | 0.9945    | 7.09           | 0.011    | 0.9990      | 4.39                       | 0.003    |  |  |
| model | Test set       | 0.9835    | 7.30           | -        | 0.9880      | 14.21                      | -        |  |  |
|       | Validation set | 0.9753    | 11.16          | -        | 0.9965      | 4.89                       | -        |  |  |
|       | Complete set   | 0.9907    | 11.16          | -        | 0.9976      | 14.21                      | -        |  |  |
| KRR   | Training set   | 0.9809    | 10.61          | 0.014    | 0.9863      | 20.93                      | < 0.001  |  |  |
| model | Test set       | 0.9646    | 8.44           | -        | 0.9708      | 15.65                      | -        |  |  |
|       | Validation set | 0.9554    | 13.08          | -        | 0.9816      | 13.27                      | -        |  |  |
|       | Complete set   | 0.9756    | 13.08          | -        | 0.9842      | 20.93                      | -        |  |  |
| DNN   | Training set   | 0.9987    | 4.11           | 34.04    | 0.9990      | 12.11                      | 70.87    |  |  |
| model | Test set       | 0.9941    | 4.00           | -        | 0.9894      | 12.53                      | -        |  |  |
|       | Validation set | 0.9847    | 8.03           | -        | 0.9985      | 5.11                       | -        |  |  |
|       | Complete set   | 0.9963    | 8.03           | -        | 0.9980      | 12.53                      | -        |  |  |

Tab. 3 shows the parameters previously defined in Section 2.5.4for evaluating the performance of regression models in the case of 150 DOE points. It shows the coefficient of determination  $R^2$ , the maximum relative error between simulated and predicted data  $R_{emax}$  of the training, test, validation and the entire dataset and the time required to train the models. To proceed with the selection of the best model to be coupled with NSGA-II, parameters related to the test set are considered. The best results for  $R^2$  and  $R_{emax}$  are highlighted in green. Especially for the two regression models SEA and  $F_{max}$  the best results belong to the DNN model. These DNN parameters also prove to be the best for the entire dataset. For this reason, it was decided to integrate this regression model with the genetic algorithm to perform multi-objective optimisation. However, it is obvious that DNN models require significantly longer training times compared to conventional regression models (several tens of seconds against milliseconds). For this reason, it is legitimate to ask whether conventional regression models

are a viable alternative to DNNs. KRR appears to be the least effective regression model for the case considered here, as it has high errors and the lowest overall regression coefficients. Conversely, the MPL and LRR models provide more convincing and comparable results. It is decided to also analyse the coupling of LRR, together with DNN, and NSGA-II, as this model has slightly lower errors with comparable  $R^2$  values.

# 3.2 Multi-Objective Optimisation though NSGA-II

The regression models were then used in the context of MOO. The main objective was to determine optimal configurations in relation to both response variables. As shown in Fig. 8, the Pareto-Optimal fronts derived from DNN and LRR metamodels, which represent non-dominated solutions, are located below and to the left of the DOE points. This positioning means achieving configurations that both minimise the maximum force and maximise the SEA. The hypervolume parameters stabilise at around 0.88 for the LRR metamodel and around 0.93 for the DNN metamodel. In both instances, the running metric stabilizes at a constant value after approximately 100 generations, indicating convergence for both models.

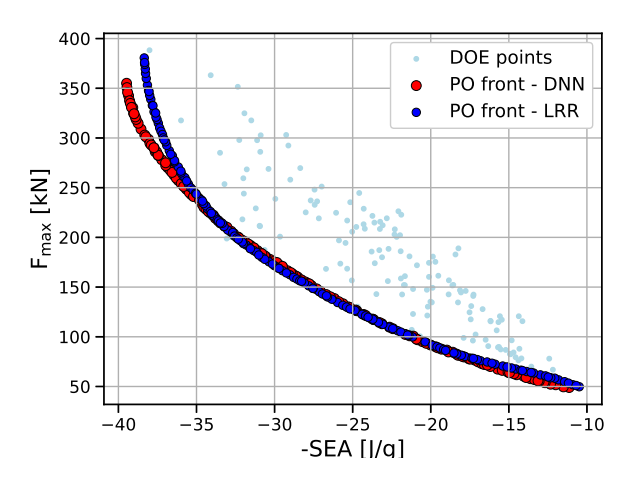


Figure 8 – Pareto-Optimal fronts from DNN and LRR coulped with NSGA-II and DOE simulation points.

To validate the accuracy of the complete surrogate model, 10 points were randomly selected along the entire PO front derived for both models. The design variables corresponding to these sample points were used to create structures that were tested with Abagus/CAE. This allowed the calculation of the errors between the values of the crash indices obtained from the simulations and those predicted by the metamodels. The results of comparing the crash indices from the simulations with those predicted by the metamodels are as follows: for the SEA test predictions using the LRR model, the maximum, mean, and minimum relative errors are 51.97%, 18.54%, and 0.44%, respectively. For the  $F_{max}$  test predictions with the same model, the maximum, mean, and minimum relative errors are 21.98%, 6.83%, and 0.42%, respectively. In contrast, the SEA test predictions using the DNN model show maximum, mean, and minimum relative errors of 5.22%, 1.39%, and 0.001%, respectively. For the  $F_{max}$  test predictions with the DNN model, the maximum, mean, and minimum relative errors are 3.22%, 2.0%, and 0.01%, respectively. The LRR metamodel encounters significant challenges in accurately predicting the parameter values in the central region of the PO front. This is likely due to the challenge of performing multivariate regression for four different variables, which the neural network excels at due to its ability to process and learn from complex datasets [18]. This allows it to overcome the limitations that often occur with classical linear and polynomial regression models. While the Pareto front offers numerous potential design solutions in the initial design phase, a final decision had to be made on the most desirable solution within this set. There are several aspects to consider when selecting this point. An initial approach was to select the two configurations that maximise the SEA and minimise the peak force and that are shown in Fig. 9 as Configuration 1 and Configuration 2, respectively. Alternatively, an optimal solution, referred to as "Knee Point" (KP)

configuration, was determined using the "Minimum Distance Selection Method" (TMDSM) [30]. The knee point usually provides an overall optimal solution in the objective space, as it is considered a balanced compromise for conflicting and competing objectives [31].

These three configurations were selected for both LRR and DNN metamodels and simulated using Abaqus/CAE. The results are shown in Fig. 9.

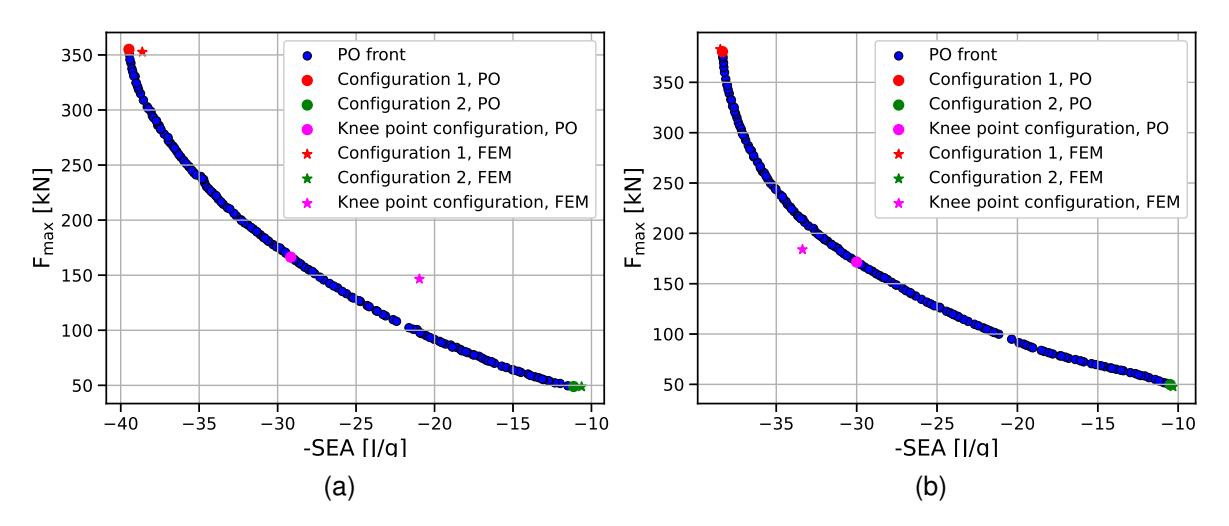


Figure 9 – PO and FEM results of selected geometry configurations for a) LRR metamodel and b) DNN metamodel.

The four geometric variables, the absorbed specific energy and the maximum crushing force with respect to the three identified configurations for both the LRR and DNN metamodels are shown in Tab. 4 for both the PO and FEM cases, with the relative errors of the response variables highlighted. In order to obtain a meaningful comparison of the crash performance parameters, the results and geometric variables obtained with C4's FEA are also shown in Tab. 4.

| Table 1   | Structural   | parameters an   | d ontimizad  | l variables e | f calacted | configurations | and of C1  |
|-----------|--------------|-----------------|--------------|---------------|------------|----------------|------------|
| 1able 4 - | - Siruciurai | i barameters an | a obiiiiizea | i vanabies o  | ı selecied | connourations  | ano oi 64. |

|                          | Conf. 1<br>(LRR) | Conf. 2<br>(LRR) | KP conf.<br>(LRR) | Conf. 1<br>(DNN) | Conf. 2<br>(DNN) | KP conf.<br>(DNN) | C4     |
|--------------------------|------------------|------------------|-------------------|------------------|------------------|-------------------|--------|
| SEA (PO) [J/g]           | 39.48            | 11.14            | 29.17             | 38.35            | 10.49            | 30.00             | -      |
| SEA (FEM)<br>[J/g]       | 38.62            | 10.63            | 20.96             | 38.48            | 10.32            | 33.37             | 32.50  |
| $R_e$ (SEA) [%]          | 2.21             | 4.76             | 39.15             | 0.35             | 1.63             | 10.11             | -      |
| Peak force<br>(PO) [kN]  | 355.04           | 48.94            | 166.45            | 380.50           | 49.73            | 171.45            | -      |
| Peak force<br>(FEM) [kN] | 352.61           | 48.80            | 146.58            | 382.76           | 47.70            | 183.93            | 285.22 |
| $R_e(F_{max})$ [%]       | 0.69             | 0.29             | 13.55             | 0.59             | 4.27             | 6.79              | -      |
| $t_w$ [mm]               | 1.0              | 1.0              | 1.0               | 1.0              | 1.0              | 1.0               | 2.55   |
| $t_c$ [mm]               | 2.5              | 1.0              | 1.99              | 2.5              | 1.0              | 1.0               | 2.55   |
| r [mm]                   | 5.29             | 2.5              | 2.62              | 5.99             | 2.51             | 3.79              | 4.0    |
| A [-]                    | 0.0              | 1.45             | 0.0               | 0.0              | 1.5              | 0.0               | 0.0    |
| Mass [g]                 | 162              | 73.9             | 98.4              | 176              | 74.1             | 98.7              | 157    |

Tab. 4 shows that both metamodels used lead to the selection of the optimal structures with similar characteristics: in order to maximise the specific energy absorption, the waviness along the height of the structure must be zero, while the values for the radius and the thickness of the reinforcing cylinders must be high. As for the reduction of the maximum force peak, the parameter A should be high, while the radius and the thickness of the reinforcing cylinders are small. However, there is no

such clearly defined trend for the KP configuration. For all three cases, the minimum possible wall thickness is identified as optimal. It can be seen that the errors are quite small when considering the DNN regression model, which has already been confirmed with the numerically tested PO sample points. The agreement between the regression models, the results of the NSGA-II genetic algorithm and the FEA values therefore underlines the effectiveness of the model in early design phases and reduces the computational resources required for structural optimisation.

Fig. 10 shows the deformation modes of the three optimised structures obtained with LRR and DNN metamodels. The LRR-KP configuration and the LRR and DNN configurations 1 exhibit a global buckling mode, where the folding deformation occurs with local buckling, resulting in the walls having larger folding wavelengths compared to the other modes [32]. Both configurations 2 instead show an asymmetric transitional collapse behaviour, where the folding deformation is randomly generated within the structure and the progressive deformation occurs alternately until the densification stage occurs, with no symmetry about any axis or plane. Due to this progressive deformation, the crushing force in the transitional mode is also less fluctuating during the plateau phase, which makes these structures suitable for energy absorbers, although predicting the initial deformation in these structures is challenging. DNN configuration 2 has a symmetric progressive deformation mode where regular lobes are generated in the walls, resulting in less fluctuation in the crushing force [20].

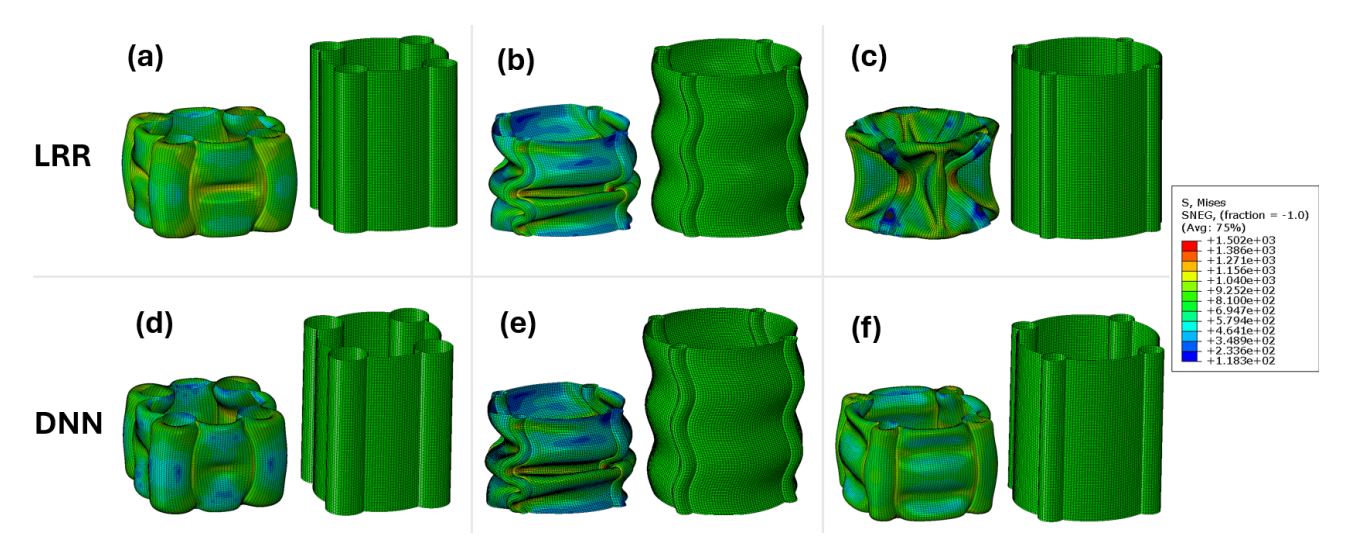


Figure 10 – Deformed and undeformed shapes of the optimized structures: (a) LRR Configuration 1, (b) LRR Configuration 2, (c) LRR KP configuration, (d) DNN Configuration 1, (e) DNN Configuration 2, (f) DNN KP configuration.

In order to gain a comprehensive understanding of the increased crashworthiness of these geometries, Abaqus/CAE simulations were carried out for reference hollow cylinders that have the same masses as the respective optimised geometries.

The diagrams in Fig. 11 show the force-displacement curves of the optimised geometries and their respective reference cylinders, while Fig. 12 present the values of the response variables for both cases and their corresponding percentage increases. The CFE,  $F_{max}$ , and SEA data presented in the figures were calculated taking into account the compression of the structures up to a length of 20 mm.

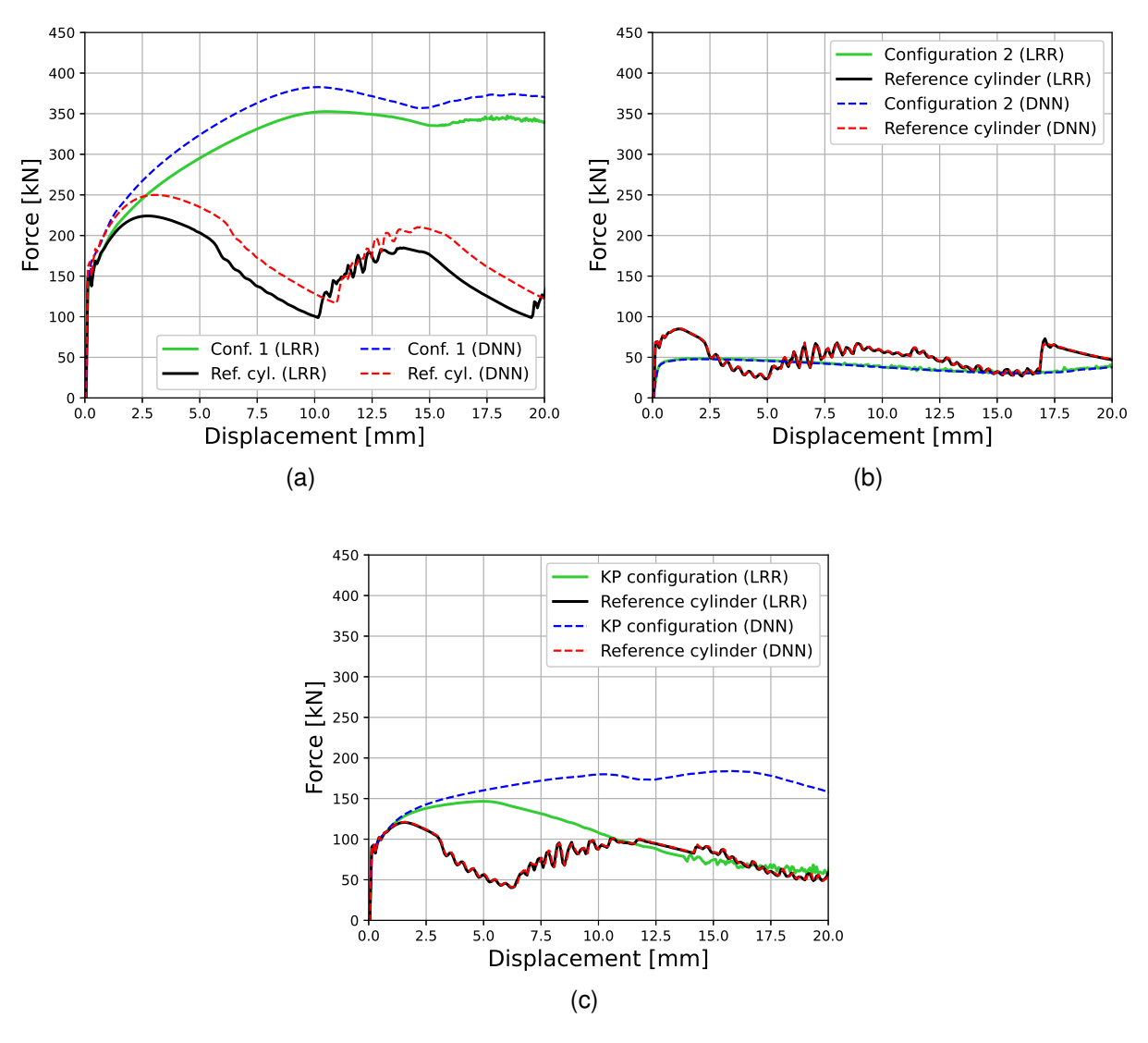
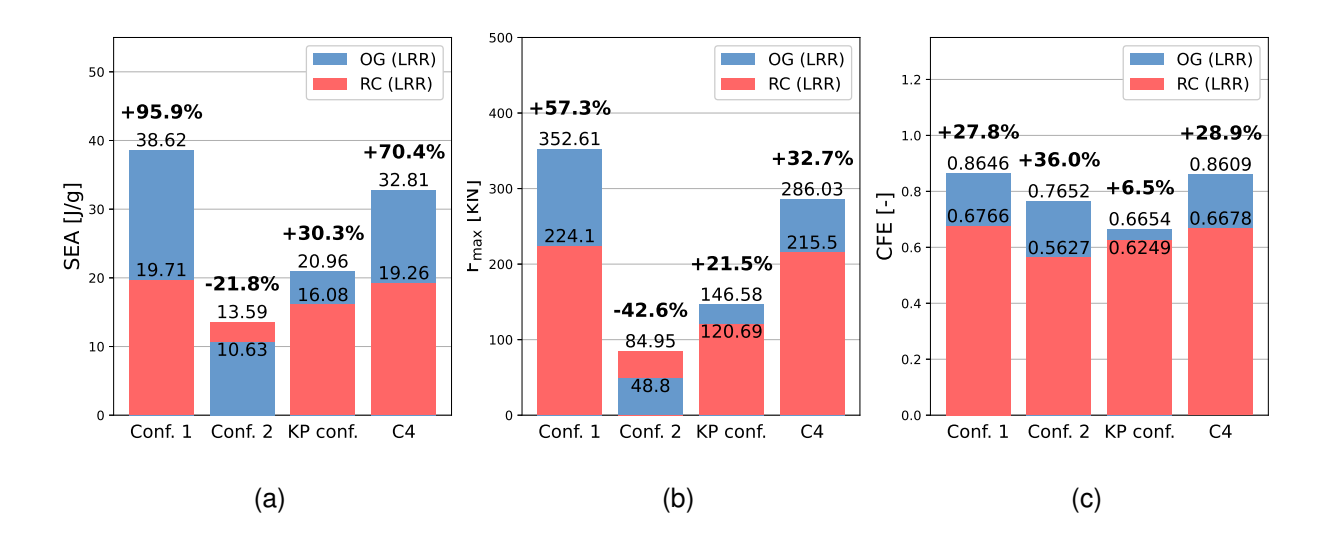


Figure 11 – Force-displacement curves comparison between selected optimized geometries and reference cylinders: a) Configuration 1, b) Configuration 2, c) Knee Point configuration



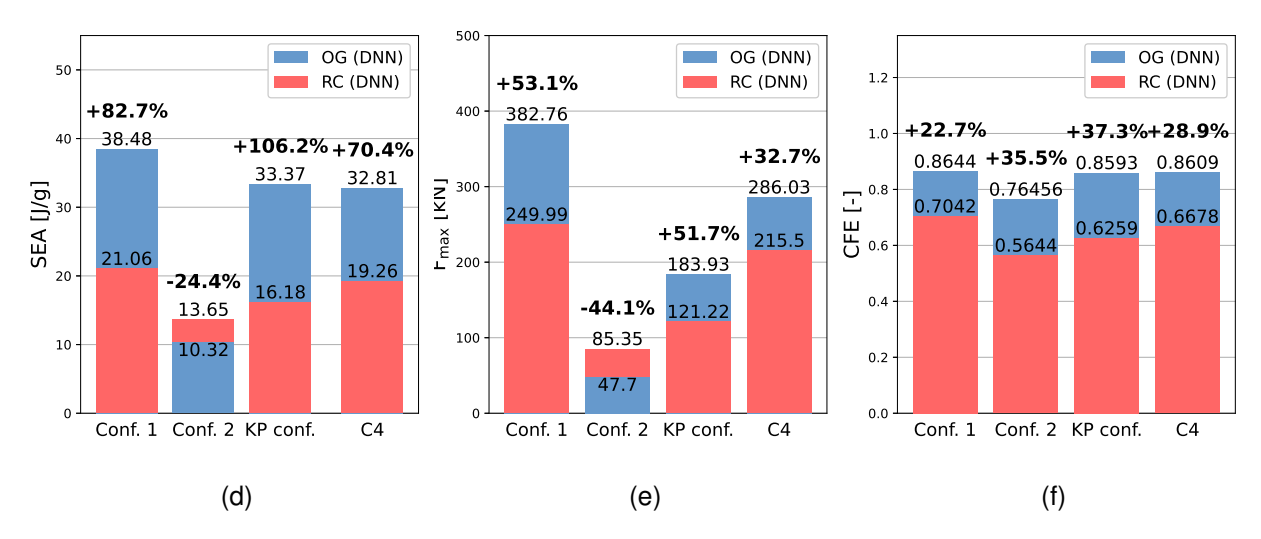


Figure 12 – Crashworthiness parameters comparison between C4 / selected optimized geometries (OG) and reference cylinders (RC) a) SEA results (LRR), b)  $F_{max}$  results (LRR), c) CFE results (LRR), d) SEA results (DNN), e)  $F_{max}$  results (DNN), f) CFE results (DNN).

As can be seen from Tab. 4 and the figures 11, 11 and 12, the solutions found by the LRR and DNN metamodels are practically identical for configuration 2 and relatively similar for configuration 1 in terms of geometrical characteristics, deformation modes and crashworthiness indices. In the case of the KP configuration, however, although the two structures identified at the PO front have very similar masses, the differences in the other defining geometrical parameters lead to completely different collapse behaviour and, consequently, to different crash parameters. As shown in Fig. 12. all optimised geometries significantly improve the properties of the base absorber while maintaining the same mass, which was already confirmed in the previous work [16], with the exception of configuration 2. Indeed, configuration 1 (Fig. 11a) shows a significant improvement of the SEA and CFE parameters for both metamodels. Despite an increase in maximum force, the high crushing efficiency of the selected geometry ensures stable occupant accelerations without significant peaks. Configuration 2 (Fig. 11b) shows a slight decrease in SEA in both cases, in contrast to what was observed in the previous work. However, the main improvements are the significant increase in CFE and the reduction in maximum force during compression. This indicates that the absorber behaves more like an ideal absorber. It achieves almost the same energy absorption as the basic geometry and at the same time reduces the risk of excessive occupant acceleration. The knee point configuration (Fig. 11c) is characterised, as one might expect from its definition, by the improvement in overall efficiency, combining increased specific absorbed energy and minimised peak force, for which the percentage increase is lower than in configuration 1. However, Fig.12 clearly shows that the configuration obtained by the DNN metamodel performs significantly better than the one obtained by LRR at almost the same mass. Overall, it shows the most significant increases in terms of the SEA and CFE values. In all four cases, the optimised geometries significantly reduce the force peaks associated with the instability of the folds in the height of the structure [33].

Finally, we compared the computational efficiency of the LRR metamodel, the DNN metamodel and the FEA for results obtained on a computer with a 13th Gen Intel(R) Core(TM) i7-1370P CPU and an Intel(R) UHD Graphics GPU. The calculation of a load curve exceeding 20 mm compression distance of these elytra-inspired configurations in FEM takes on average about 13 minutes, with a parallelisation of the tasks of each simulation on 4 processors. An evaluation of SEA and  $F_{max}$  with the LRR regression model takes on average 0.00098 s and 0.00099 s, respectively, while it takes 0.0628 s and 0.0575 s to obtain the same parameters with the DNN regression model, respectively. The difference between the two models is about 2 orders of magnitude. Looking at the computational cost required by the complete metamodel to derive the PO front (Fig. 7), it can be observed the trend of time with respect to the number of individuals in the original DOE dataset. For both the LRR model and the DNN model, the time increases with the size of the population, although it seems to reach

an asymptote around 860 s, especially in the case of the DNN metamodel. For a dataset of 150 individuals, the execution time of NSGA-II with the DNN model is 868.75 s on average, while for the LRR model it is about 5.30 s. Comparing these times with the time required to train the models, it becomes clear that the time required differs by around two orders of magnitude, as expected.

Tab. 5 shows the  $R^2$  value, separately for SEA and  $F_{max}$  regression models, of a new dataset created by adding to the original DOE dataset, consisting of 150 points, also the data of the points randomly selected to test the LRR and DNN metamodels, as well as the data of their respective optimal configurations. The table also presents the  $R^2$  values obtained from fitting two separate datasets: one consisting of SEA and  $F_{max}$  values from the FEM that are below the 10th and above the 90th percentiles, and another consisting of values between the 20th and 80th percentiles. The  $R^2$  values for the first dataset, which includes extreme values and outliers, indicate that both ML models effectively predict these extremes, with  $R^2$  values exceeding 0.99 for both SEA and  $F_{max}$ . In the second dataset, there is a pronounced discrepancy in predicting central values: the LRR-SEA regression model exhibits greater difficulty in maintaining accuracy compared to the DNN model, leading to significantly larger errors.

Table  $5 - R^2$  score of the LRR and DNN metamodels fitting of entire dataset (original entire dataset, testing points datasets and optimal configurations data).

|                 |                  |                     |                  | R <sup>2</sup> score th and above ercentiles |                  | 20th and         |
|-----------------|------------------|---------------------|------------------|--|------------------|------------------|
| ML<br>algorithm | overall<br>(SEA) | overall $(F_{max})$ | SEA              | $F_{max}$                                    | SEA              | $F_{max}$        |
| LRR<br>DNN      | 0.9585<br>0.9952 | 0.9834<br>0.9981    | 0.9955<br>0.9996 | 0.9915<br>0.9996                             | 0.8167<br>0.9906 | 0.9216<br>0.9876 |

For these reasons, although the efficiency of the DNN metamodel is lower than that of the LRR, the first option is still preferable due to its higher accuracy. Moreover, once trained, it is in any case about  $10^4$  times faster than FEA in calculating the mechanical properties of honeycomb cells. This significantly improves the process of exploring the design space.

## 4. Conclusions and future developments

In this study, an optimisation was carried out to enhance the crash performance of bio-inspired sandwich core cell structures. SEA,  $F_{max}$ , and CFE were used as measures of crashworthiness and were calculated using Explicit finite element analysis. The study started with an elytra-inspired geometry with four reinforcing cylinders (C4) selected based on the results of a previous parametric optimisation using the COPRAS method. A DOE was then formulated to proceed with a subsequent phase of multiobjective optimisation. Four regression models (MPR, LRR, KRR and DNN) were developed and tested to predict SEA and  $F_{max}$  values. After model fitting, it was decided to couple the LRR and DNN regression models with the NSGA-II genetic algorithm, as the first model had a good balance between model accuracy and excellent prediction time, while the second model had the better regression coefficients and relative errors. Subsequently, multi-objective optimisation was then performed, including as design variables the radius of the reinforcing cylinders, a sine wave parameter of a deformation line along the height, and the cylinder and wall thicknesses, with the objective of minimising the peak of the maximum force  $F_{max}$  while maximising the absorbed specific energy SEA. Two Pareto fronts were then determined and the performance of the metamodels was analysed in detail. Three optimal configurations were selected for both metamodels: Configuration 1 aiming to maximise the SEA, Configuration 2 aiming to minimise  $F_{\text{max}}$ , and the Knee Point configuration determined by the minimum distance selection method. All optimised geometries significantly improve the properties of a basic absorber while maintaining the same mass. The KP configuration derived from the DNN regression model shows the most significant increases in SEA and CFE values (+106.2% and +37.3%, respectively), with the results of the PO and FEM calculations being very close. The

calculation efficiency of the LRR metamodel, DNN metamodel and FEM is then compared. While the LRR regression model requires about  $10^-3$  s after training to evaluate a configuration and extract each crash indices, the DNN requires about 5 x  $10^-2$  seconds. As a result, the computation time for the complete run of the metamodel for the DNN (868.7 s) is two orders of magnitude higher than for the LRR (5.3 s). However, looking at the  $R^2$  obtained by fitting the values corresponding to the extremes of the crash parameters and the intermediate values, it becomes clear that the combined DNN / NSGA-II metamodel achieves a significantly higher accuracy compared to the LRR one. Moreover, once trained, it is about  $10^4$  times faster than FEA in calculating the mechanical properties of honeycomb cells.

It can be concluded that the coupling of NSGA-II and a neural network regression model with FEM analysis has proven to be effective for structural multi-objective optimisation in an initial design phase. The metamodel can predict the values much faster compared to a traditional numerical test while reducing the errors between predicted and numerical values compared to more traditional regression methods used for metamodels.

Future developments of this research should focus on designing a complete honeycomb panel to study bending effects and the interactions between the walls of the structure. The inclusion of a genetic algorithm that can handle more than two response variables for many-objective optimisation could be beneficial in identifying even better performing structures.

## **Contact Author Email Address**

Corresponding author: Bianca Omede', email: bianca.omede@polimi.it

Antonio Mattia Grande, email: antoniomattia.grande@polimi.it

# **Copyright Statement**

The authors confirm that they, and/or their company or organization, hold copyright on all of the original material included in this paper. The authors also confirm that they have obtained permission, from the copyright holder of any third party material included in this paper, to publish it as part of their paper. The authors confirm that they give permission, or have obtained permission from the copyright holder of this paper, for the publication and distribution of this paper as part of the ICAS proceedings or as individual off-prints from the proceedings.

## References

- [1] N. San Ha, G. Lu. A review of recent research on bio-inspired structures and materials for energy absorption applications. *Composites Part B: Engineering*, Vol. 181, 2020.
- [2] A.G. Olabi, E. Morris, M.S.J. Hashmi. Metallic tube type energy absorbers: A synopsis. *Thin-Walled Structures*, Vol. 45, No. 7, pp 706-726, 2007.
- [3] W. Zhang, J. Xu, T. Yu. Dynamic behaviors of bio-inspired structures: design, mechanisms, and models. *Engineering Structures*, Vol. 265, 2022.
- [4] K. Günaydın, Z. Eren, Z. Kazancı, F. Scarpa, Fabrizio, A.M. Grande, H.S. Türkmen. In-plane compression behavior of anti-tetrachiral and re-entrant lattices. *Smart Materials and Structures*, Vol. 28, No. 11, 2019.
- [5] EPMA. Introduction to Additive Manufacturing Techonlogy. 3rd edition, EuroAM, 2019.
- [6] A. Ingrole, T.G. Aguirre, L. Fuller, S.W. Donahue. Bioinspired energy absorbing material designs using additive manufacturing. *Journal of the mechanical behavior of biomedical materials*. Vol. 119, 2021.
- [7] J. Fang, G. Sun, N. Qiu, N.H. Kim, Q. Li. On design optimization for structural crashworthiness and its state of the art. *Structural and Multidisciplinary Optimization*. Vol. 55, pp. 1091–1119, 2017.
- [8] C.P. Kohar, L. Greve, T.K. Eller, D.S. Connolly, K. Inal. A machine learning framework for accelerating the design process using CAE simulations: An application to finite element analysis in structural crashworthiness, *Computer Methods in Applied Mechanics and Engineering*. Vol. 385, 2021.
- [9] N. Qiu, Y. Gao, J. Fang, Z. Feng, G. Sun, Q. Li. Crashworthiness analysis and design of multi-cell hexagonal columns under multiple loading cases. *Finite Elements in Analysis and Design*. Vol 104, pp. 89-101, 2015.
- [10] F. Tarlochan, F. Samer, A.M.S. Hamouda, S. Ramesh, K. Khalid. Design of thin wall structures for energy absorption applications: Enhancement of crashworthiness due to axial and oblique impact forces. *Thin-Walled Structures*. Vol. 71, pp.7-17, 2013.
- [11] A. Bigdeli, M.D. Nouri. A crushing analysis and multi-objective optimization of thin-walled five-cell structures. *Thin-Walled Structures*. Vol 137, pp. 1-18, 2019.

- [12] W. Guo, P. Xu, C. Yang, J. Guo, L. Yang, S. Yao, Shuguang. Machine learning-based crashworthiness optimization for the square cone energy-absorbing structure of the subway vehicle. *Structural and Multi-disciplinary Optimization*. Vol. 66, 2023.
- [13] L. Lanzi, C. Bisagni, S. Ricci. Neural network systems to reproduce crash behavior of structural components, *Computers & Structures*, Vol. 82, pp. 93-108, 2004.
- [14] M.R. Faraz, S. Hosseini, A. Tarafdar, M. Forghani, H. Ahmadi, N. Fellows, G. Liaghat. Crashworthiness behavior assessment and multi-objective optimization of horsetail-inspired sandwich tubes based on artificial neural network, *Mechanics of Advanced Materials and Structures*. 2023.
- [15] F.E. Carakapurwa, S.P. Santosa. Design optimization of auxetic structure for crashworthy pouch battery protection Using Machine Learning Method. *Energies*. 2022.
- [16] B. Omede', A.M. Grande. Parametric optimization of bio-inspired engineered sandwich core. *Materials TodayCommunications*. Vol. 39, 2024.
- [17] P. Hao, J. Du. Energy absorption characteristics of bio-inspired honeycomb column thin-walled structure under impact loading *Journal of the Mechanical Behavior of Biomedical Materials*. Vol 79, pp. 301-308, 2018.
- [18] A.I. Pais, J. Belinha, J.L. Alves. Advances in computational techniques for bio-inspired cellular materials in the field of biomechanics: Current trends and prospects. *Materials*. Vol. 16, no. 11, 2023.
- [19] E.K. Zavadskas, A. Kaklauskas, V. Šarka. The new method of multicriteria complex proportional assessment of projects. *Technological and Economic Development of Economy*. Vol. 1, pp. 131-139, 1994.
- [20] N. San Ha, T. M. Pham, H. Hao, G. Lu. Energy absorption characteristics of bio-inspired hierarchical multi-cell square tubes under axial crushing. *International Journal of Mechanical Sciences*. Vol. 201, 2021.
- [21] D.C. Montgomery. Design and analysis of experiments. 9th edition, John Wiley & Sons, 2017.
- [22] R. Qin, J. Zhou, B. Chen. Crashworthiness design and multiobjective optimization for hexagon honeycomb structure with functionally graded thickness. *Advances in Materials Science and Engineering*. Vol. 2019, pp. 1-13, 2019.
- [23] X. Yu, X. Zhang, J. Chen, L. Pan, Y Xu, Y. Fu. Experimental verification and optimization research on the energy absorption abilities of beetle elytron plate crash boxes. *Materials Research Express*. Vol.6, 2019.
- [24] L. Musenich, A. Stagni, L. Derin, F. Libonati. Tunable energy absorption in 3D-printed data-driven diatom-inspired architected materials. *ACS Materials Letters*. Vol6, no.6, pp. 2213-2222.
- [25] A.A. Alkhouly, A. Mohammed, H.A. Hefny. Improving the performance of deep neural networks using two proposed activation functions. *IEEE Access*. Vol. 9, pp. 82249-82271, 2021.
- [26] H. Yin, Y. Xiao, G. Wen, Q. Qing, X. Wu. Crushing analysis and multi-objective optimization design for bionic thin-walled structure. *Materials & Design*. Vol. 87, pp. 825-834, 2015.
- [27] K. Deb, A. Pratap, S. Agarwal, T. Meyarivan. A fast and elitist multiobjective genetic algorithm: NSGA-II. *IEEE Transactions on Evolutionary Computation*. Vol. 6, no. 2, pp. 182-197.
- [28] J. Zhang, G. Sun, G. Li, Z. Luo, Q. Li, Optimization of foam-filled bitubal structures for crashworthiness criteria. *Materials & Design*. Vol. 38, pp.99-109, 2012.
- [29] J. Blank, K. Deb. Pymoo: Multi-objective optimization in Python. *IEEE Access*. Vol.8, pp. 89497-89509, 2020.
- [30] G. Sun, G. Li, S. Zhou, H. Li, S. Hou, Q. Li, Crashworthiness design of vehicle by using multiobjective robust optimization. *Structural and Multidisciplinary Optimization*. Vol. 44, pp. 99-110, 2011.
- [31] J. Branke, K. Deb, H. Dierolf, M. Osswald. Finding knees in multi-objective optimization. *Parallel Problem Solving from Nature PPSN VIII*, pp.722-731, 2004.
- [32] J. Legendre, P. Le Grognec, C. Doudard, S. Moyne. Analytical, numerical and experimental study of the plastic buckling behavior of thick cylindrical tubes under axial compression, *International Journal of Mechanical Sciences*. Vol. 156, pp. 494–505, 2019.
- [33] J. Marsolek, H.G. Reimerdes. Energy absorption of metallic cylindrical shells with induced non-axisymmetric folding patterns. *International Journal of Impact Engineering*. Vol. 30, no.8-9, pp.1209-1223,2004.